Heliyon 10 (2024) e31351

Contents lists available at ScienceDirect

Heliyon

journal homepage: www.cell.com/heliyon

Research article

Facile synthesis of TiO_2@ZnO nanoparticles for enhanced removal of methyl orange and indigo carmine dyes: Adsorption, kinetics

Mohamed Ali Ben Aissa [a], M. Khairy [b,c,*], Magdi E. Khalifa [d], Ehab A. Abdelrahman [b,c], Nadeem Raza [b], Emad M. Masoud [e,**], Abueliz Modwi [a]

[a] Department of Chemistry, College of Science, Qassim University, P. O. Box: 6644, Buraydah 51452, Saudi Arabia
[b] Chemistry Department, College of Science, Imam Mohammad Ibn Saud Islamic University (IMSIU), Riyadh 11623, Saudi Arabia
[c] Chemistry Department, Faculty of Science, Benha University, Benha 13518, Egypt
[d] Department of Chemistry, Faculty of Science, Mansoura University, Mansoura 35516, Egypt
[e] Department of Chemistry, Faculty of Science, Islamic University of Madinah, 42351, Madinah, Saudi Arabia

ARTICLE INFO

Keywords:
TiO_2@ZnO nanocomposites
MO and IC dyes removal
Kinetics
pH impact
Mechanism

ABSTRACT

Water pollution represents one of the most important problems affecting the health of living organisms, so it was necessary to work on the formation of active materials to get rid of pollutants. In this study, Titanium dioxide (TiO_2) doping Zinc oxide (ZnO) nanocomposites were produced via simple sonication method at 500 Hz in ethanol medium. At different weight concentrations (2.5, 5, 7.5, and 10 %). The morphology, structure configuration, chemical bonding, crystalline phase, and surface properties of obtained nanocomposites were characterized via FESEM, BET, XRD, XPS, RAMAN and FTIR instrumentation. The nanocomposites were employed as an adsorbent to eliminate the methyl orange (MO) and Indigo Carmine (IC) dyes from an aqueous solution. Batch removal experiments revealed that the elimination of MO and IC dyes by the TiZnO surface was pH and doping Ti concentration-dependent, with maximum removal occurring at pH = 7 for MO and pH = 3 for IC contaminants at 10 % doping Ti concentration (Ti (10 %)@ZnO). Langmuir model fit the absorptive removal of MO and IC dyes into the Ti (10 %)@ZnO surface well. The maximal removal capacity of Ti (10 %)@ZnO nanocomposite was found to be 994.24 mg. g^{-1} for MO and 305.39 mg. g^{-1} for IC. The Ti (10 %)@ZnO nanocomposite showed remarkable high stability towards the removal of both dyes through consecutive four cycles.

1. Introduction

Industrial and municipal wastewater discharge without sufficient environmental treatment pollutes pristine water supplies, causing many health and environmental problems [1,2]. Pharmaceutical products, phenolic species, pesticides, synthetic dyes, and heavy metals are examples of contaminants that exist in wastewater [3]. The impact of dyes and other organic pollutants on water resources and the overall environment is significant [4,5]. The unauthorized release of dyes and various organic pollutants can have a

* Corresponding author. Chemistry Department, College of Science, Imam Mohammad Ibn Saud Islamic University (IMSIU), Riyadh 11623, Saudi Arabia.
** Corresponding author.
E-mail addresses: mkomran@imamu.edu.sa (M. Khairy), emad.youssef@iu.edu.sa (E.M. Masoud).

https://doi.org/10.1016/j.heliyon.2024.e31351
Received 7 January 2024; Received in revised form 7 May 2024; Accepted 15 May 2024
Available online 16 May 2024

detrimental effect on the quality of air, soil, and natural water resources [6]. The presence of non-degradable organic materials has the potential to disrupt the food chain of aquatic flora and fauna, leading to the mortality of fish, algae, and other aquatic species, ultimately resulting in the collapse of the entire ecological system [7,8]. Dyes have been identified as one of the harmful organic pollutants that require immediate attention due to their chemical composition [9]. Dyes in water bodies are mostly caused by effluent from the leather, printing, paints, plastics, rubber, paper, and textile industries [10]. Dyes are classed according to their charge, functional groups, and usability. They can be classed as cationic dyes, anionic dyes, and nonionic dyes, depending on their chemical structures [11]. Methyl orange (MO) is an acidic anionic mono-azo dye ($C_{14}H_{14}N_3SO_3Na$, 327.34 g/mol) that is widely and indefinitely employed in textiles, laboratory studies, and other commercial items [12–14]. This dye is hazardous to aquatic life [15]. Acute exposure to this hazardous dye can result in increased heart rate, vomiting, shock, cyanosis, jaundice, quadriplegia, and tissue necrosis in humans [16]. Indigo carmine (IC), often known as acid blue, is an anionic dye with the chemical formula 3,3-dioxi-2,2-bis-indilyden-5,5-disulfonic acid sodium salt ($C_{16}H_8N_2Na_2O_8S_2$, 466.36 g/mol) with four aromatic rings [17]. It is used as a dyeing substance for various applications, including textile coloring, cosmetics, printing, biological staining, dermatological and antibacterial agents, and as a chicken feed addition [18]. It is a strong toxin to mammalian cells, an irritant, a recalcitrant, and has a high coloring capability in aqueous solutions [19–21].

Coagulation, chemical oxidation, microbiological treatment, electrochemical oxidation, photo-degradation, and adsorption are regularly used separation techniques for removing dyes from wastewater [22–25]. The adsorption process is widely used because of its advantageous characteristics, such as simplicity of operation, high-performance effectiveness, more recoverability, greater accessibility to adsorbates, and reduced secondary pollution and low cost [26,27]. This enables the total removal of all unwanted substances without changing their molecular structure.

One of the most important ways to improve water treatment methods is to use nanoscale materials that have the ability to adsorption, as nanoscale materials have several properties that help them adsorb the organic molecules that make up dyes [28]. Because of its high electron mobility, direct bandgap, anisotropic growth, high chemical stability, high adsorption capability, high photocatalytic effectiveness, and ease of morphological control, zinc oxide (ZnO) is a valuable material for the removal of pollutants from water [29,30].

Powdered titanium dioxide (TiO_2) is regarded by many as one of the most significant materials used in semiconductors [31]. Because the band gap of nanoparticles increases with decreasing size and small TiO_2 particles provide a very large surface area, nanosize TiO_2NPs have a number of special properties [32]. Because of their chemical and physical stability, huge surface area, resistance to corrosion, non-toxicity, comparatively low cost, and stable colloidal suspension, TiO_2 nanostructures offer high sustainable efficiency [33]. In the ZnO lattice, interstitial or substitutional Zn^{2+} ions are replaced by Ti^{4+} ions. This can lead to a weakening of oxygen bonds, which in turn causes oxygen to depart and create oxygen vacancies. These vacancies can then cause water to adsorb and dissociate, creating a high OH density at the surface that can encourage photoactivity, superhydrophilicity, and the adsorption of organic dyes.

Nonetheless, most research on Zn doping with TiO_2 has concentrated solely on the structural, optical, and photocatalytic features [34–36]. However, the adsorption properties are not investigated. In this regard, Ti (2.5, 5, 7.5, and 10 %) doped ZnO nansorbents were obtained using a simple sonication method and were used as a sorbent for IC and MO dyes.

2. Experimental methods

2.1. Materials

Titanium (IV) oxide (TiO_2, ≥99.0 %), tartaric acid $(CHOH–COOH)_2$, ≥99.0 %), Zinc acetate dihydrate $(Zn(CH_3COO)_2, 2H_2O$, ≥99.0 %), sodium hydroxide (NaOH, ≥99 %), gelatin (≥90.0 %) Methyl orange (MO, ≥90 %), indigo carmine (IC ≥ 90 %), hydrochloric acid (HCl, ≥37 %), and ethanol (C_2H_5OH, ≥99 %) were purchased from Merck Company. By diluting dye stock solution (200

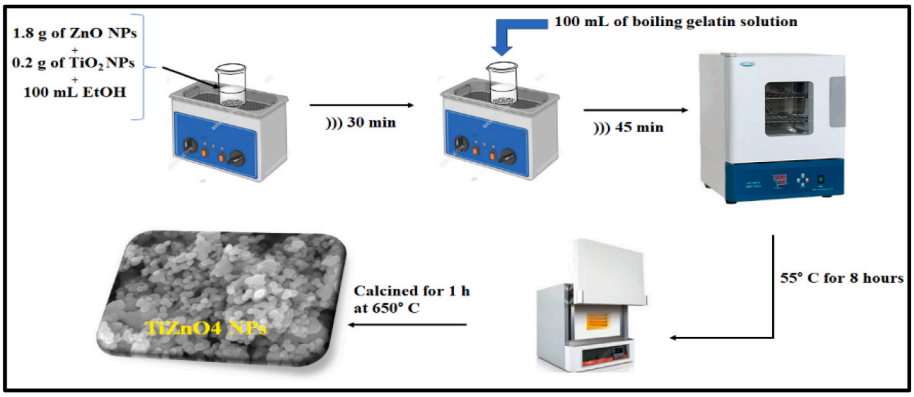

Scheme 1. Fabrication process of Ti (10 %)@ZnO nano-sorbent.

mg/L), the proper dye concentrations (7.5–100 mg/L) were obtained.

2.2. Synthesis of TiO_2@ZnO nanocomposites

The ZnO NPs were obtained following a process reported previously [37]. 10 g of zinc acetate dehydrate was dissolved in 100 mL of ethanol. After stirring for 30 min, 45 mL of tartaric acid was added dropwise. After 5 min, the gel was fast-formed at ambient temperature with intense magnetic stirring and subsequently dried at 85 °C for 16 h. Following that, the desiccated gel was initially crushed and subjected to annealing at a temperature of 550 °C for a duration of 1 h.

The TiO_2@ZnO nanocomposites were synthesized by adding TiO_2 at different weight concentrations (2.5, 5, 7.5, and 10 %) to ZnO nanoparticles. For example, for synthesizing TiO_2@ZnO nanocomposites at 10 % of weight concentrations, 0.2 g of TiO_2 NPs was added to 1.8 g of ZnO NPs. The mixture was sonicated at 500 Hz after being distributed in 100 mL of EtOH for 30 min at 25 °C until the formation of a milky solution. Under vigorous stirring, the resulting solution was gradually added to 100 mL of boiling gelatin solution. Following 45 min of sonication, the mixture was then dried in the oven for 8 h at 55 °C. After that, a muffle furnace was used to calcine the dried samples for 60 min at a temperature of 650 °C. Ti (2.5 %)@ZnO, Ti (5 %)@ZnO, Ti (7.5 %)@ZnO, and Ti (10 %)@ZnO were

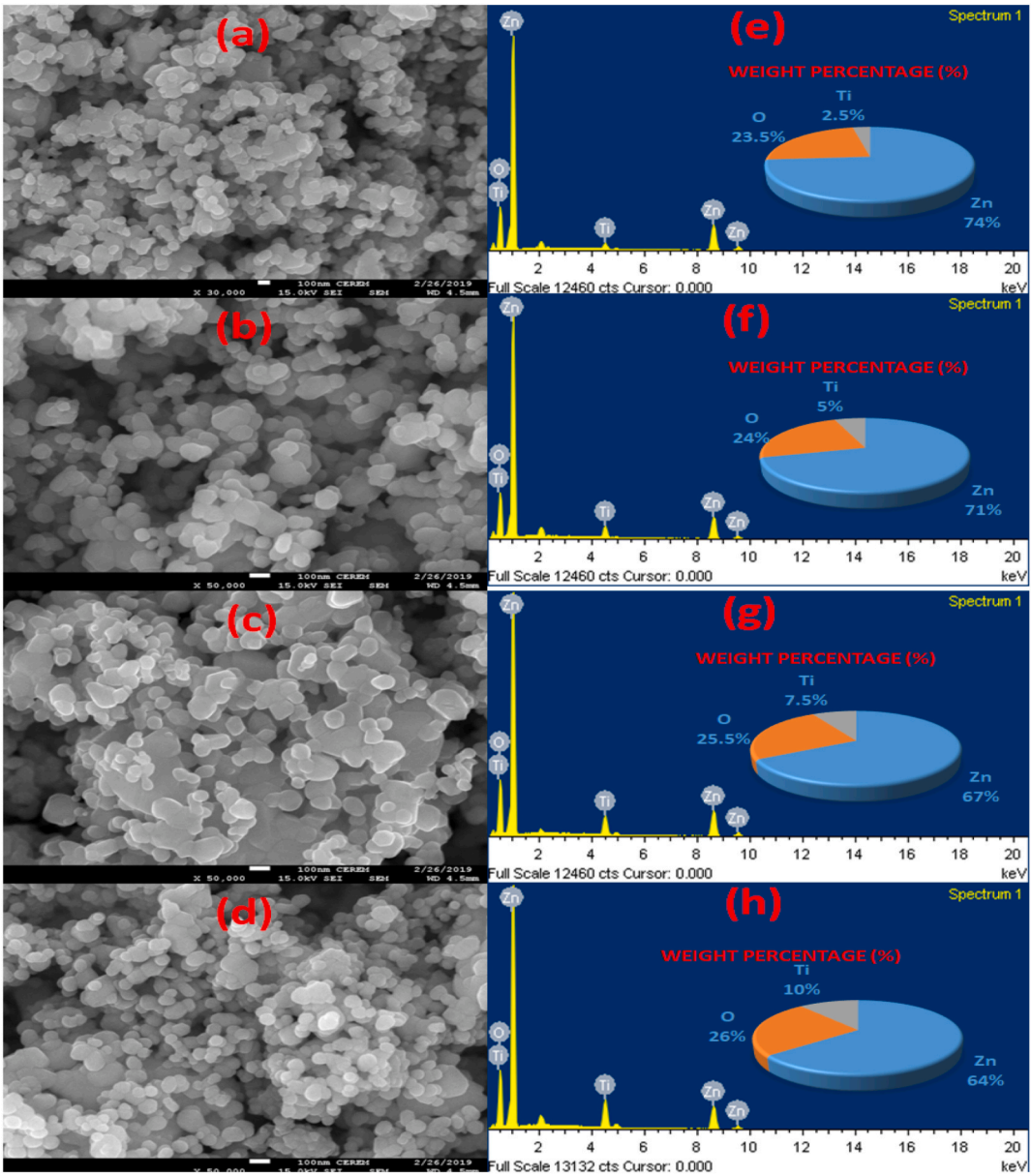

Fig. 1. SEM and EDX images of Ti (2.5 %)@ZnO (a, e), Ti (5 %)@ZnO (b, f), Ti (7.5 %)@ZnO (c, g), and Ti (10 %)@ZnO (d, h).

used to denote samples containing 2.5, 5, 7.5, and 10 % of TiO_2. Scheme 1 illustrates the fabrication procedure for Ti (10 %)@ZnO nanocomposite.

2.3. Nanocomposite characterization

The nanocomposites' morphology was studied using JEOL's JEM-2100 field emission scanning electron microscopy (FE-SEM). Using Al K (1486.6 eV) monochromatic irradiation as a reference, the chemical bonding forms of the nanomaterials were investigated using a Thermo Scientific X-ray Photoelectron Spectrometer. Using the ASAP 2020 Micromeritics device, the Brunauer-Emmett-Teller specific surface area (BET) was calculated. And N_2 adsorption-desorption isotherms. X-ray powder diffraction (XRD) was employed to examine the crystalline structure of the nanocomposites using a Bruker high-resolution diffractometer, running using Cu-Ka radiation:1.5418 Å at 40 kV7. Raman spectroscopy study was performed using a Thermo Nicolet Dispersive instrument. All nanocomposites' vibration modes were documented using a JASCO FI-IR 460 spectrometer.

2.4. MO and IC adsorption procedure

The dye concentration in textile wastewater can reach 64.6 mg/L [38]. Then, the MO and IC equilibrium elimination experiment was realized in a glass vial with a capacity of 25 mL that holds 25 mL of dye solutions at various concentrations (7.5, 15, 30, 50, 75, and 100 mg/L) and 10 mg of nano-sorbent, which were stirred for 1440 min. The mixture was centrifuged and separated after the elimination equilibrium investigation to assess the residual adsorbate concentrations. The equilibrium capacities of MO or IC dye, denoted as Q_e was determined by the following formula (Eq. 1) [39]:

$$Q_e = \frac{V}{w}(C_i - C_e) \tag{1}$$

wherein Q_e (mg. g^{-1}) signifies the adsorbates's capability to be eliminated by the mass of nanopowders, C_e denotes the equilibrium adsorbate concentrations in mg/L, W is the mass of adsorbent (g), V is the solution volume (L), and Ci is the initial concentrations of dye in solutions (mg/L).

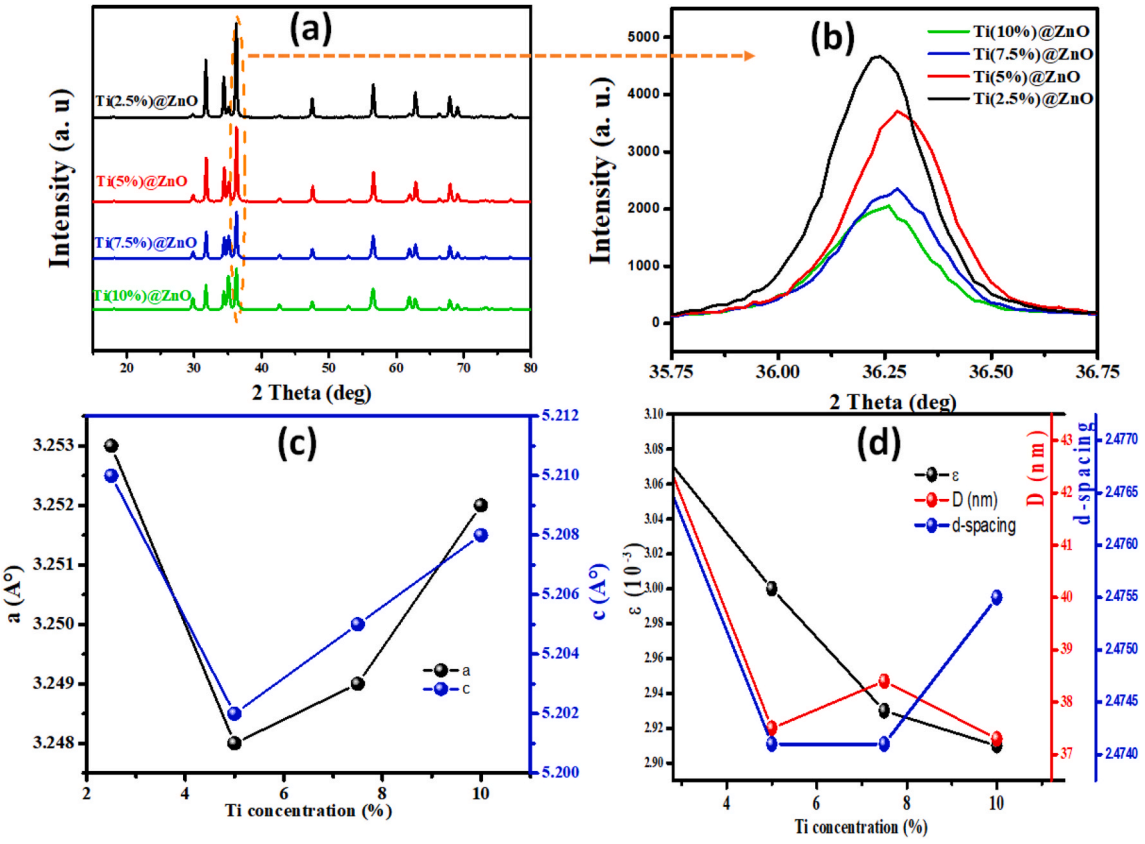

Fig. 2. (a)XRD patterns of Ti doped ZnO nanocomposites, (b) zoomed view of the (002) XRD peak (c) Ti doping concentration relies on lattice parameters, and (d) crystallite size (D), strain (ε), and Average d spacing.

The adsorption approach was utilized to measure the rate of MO and IC removal by a TiO_2@ZnO nanocomposites. To assess the contact time and kinetics, 150 ml of dyes solution were mixed with 60 mg of TiO_2@ZnO nano-sorbent at an initial concentration of 50 mg/L. A small volume of suspension was taken out at predetermined time intervals and centrifuged to assess the concentration of residual dye. Apply the following formulae (Eq. 2) to calculate the quantity of MO and IC separated per gram of sorbent nano-sorbent at each interval (min) [40]:

$$Q_t = \frac{V}{w}(C_i - C_t) \tag{2}$$

Where C_t is the dye concentrations in solutions (mg/L) at each time t (min) and Q_t (in mg. g^{-1}) is the capability of adsorbates to be eliminated per mass of nano-sorbent (w (g)) at each time t (min).

3. Results and discussions

3.1. TiZnO nanosorbent characteristics

The surface morphologies of the prepared nanocomposites are examined using SEM micrographs. Fig. 1a–d shows SEM images of the prepared nanocomposites. The SEM images reveal the nanoscale growth of Ti (2.5 %)@ZnO, Ti (5 %)@ZnO, Ti (7.5 %)@ZnO, and Ti (10 %)@ZnO. It can be seen in Fig. 1a that the Ti (2.5 %)@ZnO sample has a mixture of hexagonal and spherical particles with a size distribution ranging from 80 to 100 nm. According to the SEM images of the Ti (5 %)@ZnO and Ti (7.5 %)@ZnO specimens (Fig. 1b and c), the nanoparticles have been changed into fused oval shapes with a size distribution ranging from 50 to 80 nm. The SEM image of Ti (10 %)@ZnO (Fig. 1d) shows a decrease in particle size. The substitution of the Zn^{2+} (74 p.m.) with the Ti^{4+} (64 p.m.) with a smaller radius is probably responsible for the reduction in particle size seen in the sample with the greatest Ti ratio. The EDX spectra of the produced nanocomposites (Fig. 1e–h) demonstrate the presence of Zn, Ti, and O with no additional component, confirming the purity of the obtained nanocomposites. The percentages examination of Ti, Zn, and O in the nanocomposites is shown in the insert of Fig. 1e–h.

As shown in Fig. 2 a, the X-ray diffraction (XRD) patterns are registered to investigate the structural properties of the obtained TiO2-doping ZnO nanoparticles (2.5, 5, 7.5 and 10 %). The structural characteristics of the obtained Ti-doped ZnO nanoparticles are studied using X-ray diffraction (XRD) patterns, as illustrated in Fig. 2a. The XRD patterns of the Ti-doping ZnO nanoparticles demonstrate sharp and distinct diffraction peaks at $2\theta = 69°, 68°, 66°, 62°, 56°, 47°, 36°, 34°$, and $31°$ that can be assigned to the (202), (004), (201), (112), (200), (103), (110).

(102), (101), (002), and (100) planes confirmed the wurtzite hexagonal ZnO structure with a $P6_3mc$ space group, in agreement with JCPDS card No 36–1451 [41]. The peak corresponding to the (101) plane has the maximum strength among all detected peaks, indicating the preferred c-axis orientation [42]. Fig. 2 b shows that the peak at $2\theta = 36.24°$ for Ti (2.5 %)@ZnO shifts with doping to the higher angles. The most significant shift is observed for Ti (7.5 %)@ZnO ($2\theta = 36.76$). However, when the Ti-doping concentration

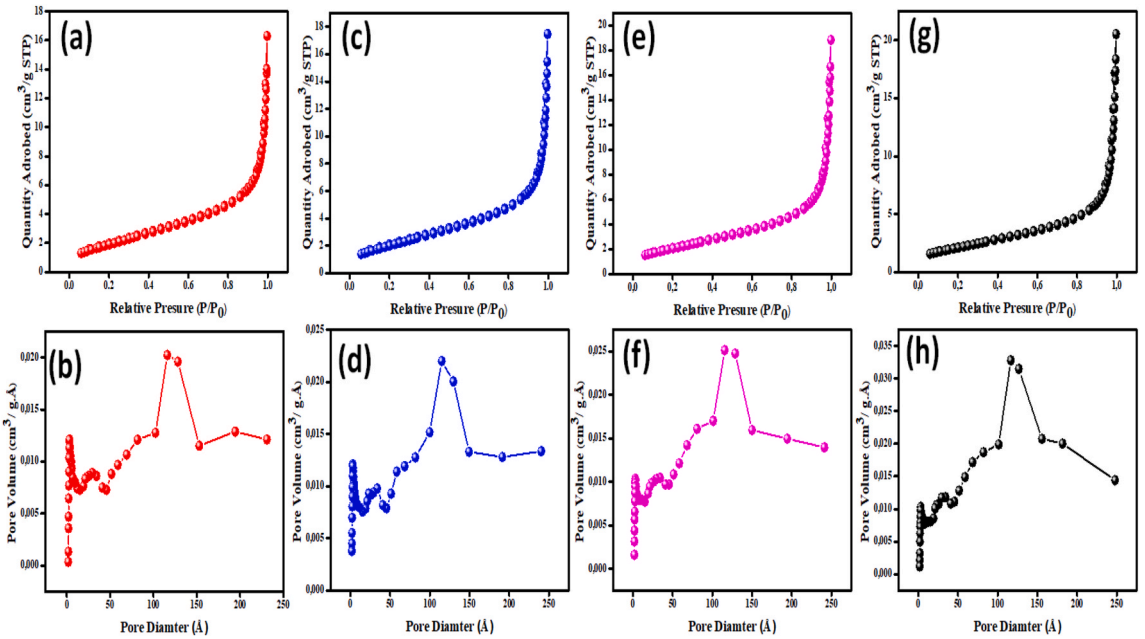

Fig. 3. N_2 sorption-desorption isotherms and the pore size distribution curve of Ti (2.5 %)@ZnO (a, b), Ti (5 %)@ZnO (c, d), Ti (7.5 %)@ZnO (e, f), and Ti (10 %)@ZnO (g, h).

increases by 10 %, the peak shift back, and the peak position becomes 2θ = 36.71. The above results show that up to 7.5 % doping concentration, Ti^{4+} replace interstitial or substitutional Zn^{2+} in the lattice of ZnO [43]. Also, Ti-doping affects the full width at half maximum (β) of XRD patterns. These changes, in turn, are known to influence the average crystallite size (D), which are determined using the Scherer and Williamson-Hall equations (Eq. 3), d-spacing (Eq. (4)), lattice parameters (a, c) (Eq. (5)), and the strain (ε) values (Eq. (6)), and given as:

$$D = \frac{0.9\lambda}{\beta \cos\theta} \text{ and } \quad \beta_{hkl} \cos\theta = \frac{K''\lambda}{D_{XRD}} + 4\varepsilon \sin\theta \tag{3}$$

$$d = \frac{\lambda}{2 \sin\theta} \tag{4}$$

$$a = \frac{\lambda}{\sqrt{3}\sin\theta} \text{ and } c = \frac{\lambda}{\sin\theta} \tag{5}$$

$$\varepsilon = \frac{\beta}{4 \tan\theta} \tag{6}$$

As a result, the values of lattice parameters (a and c) (Fig. 2 c), crystallite size (D), strain (ε), and d spacing (Fig. 2 d) are displayed versus Ti doping concentration. As depicted in Fig. 2 c, up to 6 %, the a and c values drop as the concentration of Ti-doping increases, after which these values increase at 7.5 and 10 % Ti-doping concentration. Fig. 2d demonstrates that the values of crystallite size, and d spacing do not vary noticeably with increasing Ti-doping concentration. However, Fig. 2d shows that the smallest D value (37.3 nm) was obtained for Ti (10 %)@ZnO. In addition, it is evident that the strain value (ε) consistently decreased as the titania loading increased, possibly due to the diffusion of atoms during the substitution of Zn^{2+} with Ti^{4+} throughout the nanocomposite's production [44].

Because of their direct impact on adsorbate retention abilities, the pore size and surface area of nano-sorbents are critical parameters that influence the efficacy of sorbents. Fig. 3 depicts the N_2 sorption-desorption isotherms and the corresponding distributions of pore size for the produced nanomaterials Ti (2.5 %)@ZnO (Fig. 3a and b), Ti (5 %)@ZnO (Fig. 3c and d), Ti (7.5 %)@ZnO

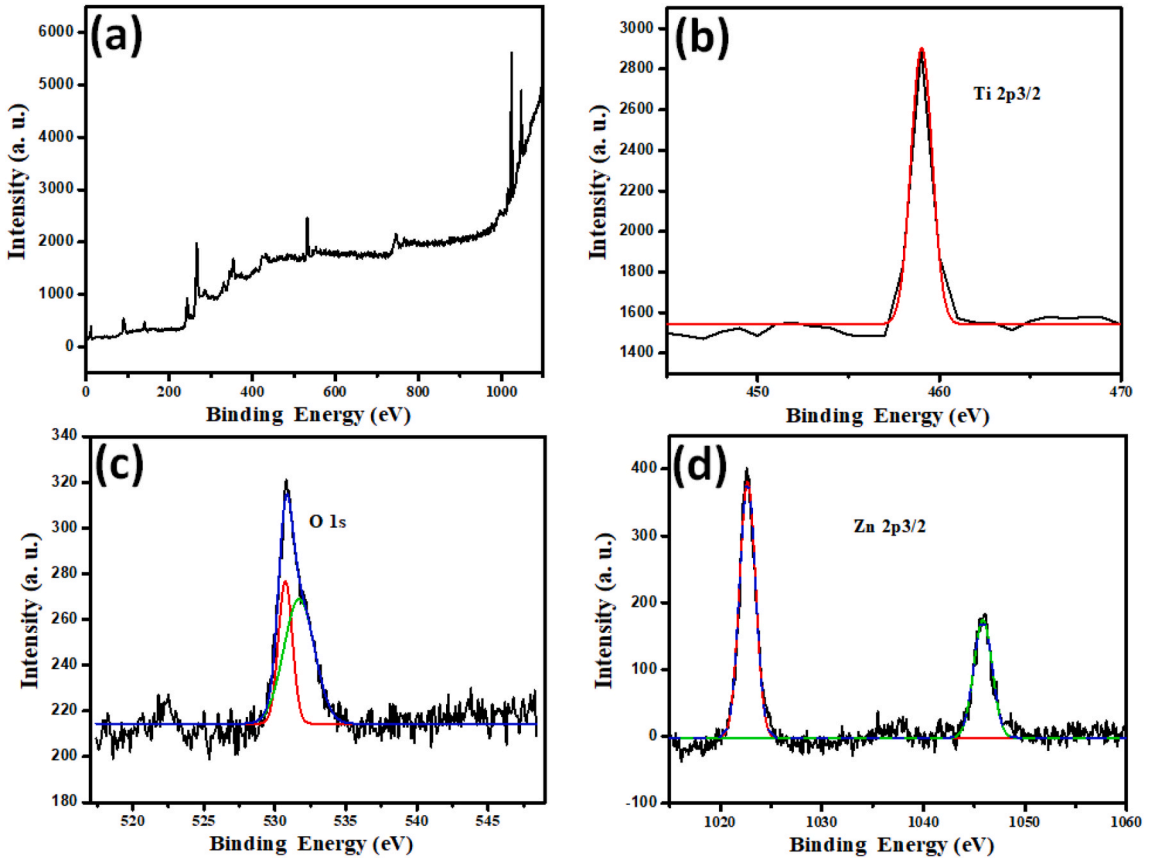

Fig. 4. XPS spectra of Ti (10 %)@ZnO nanocomposites (a) full survey and individual spectra of (b) Ti 2p3/2, (c) O1s, and (c) Zn 2p3/2.

(Fig. 3e and f), and Ti (10 %)@ZnO (Fig. 3g and h). The IUPAC classifies N_2 adsorption isotherms as Langmuir type IV with a type H3 hysteresis loop [45]. The specific surface area is increased by increasing Ti-doping concentration. The BET surface area of obtained nanocomposites are 14.7, 14.9, 15.3, and 15.5 m^2/g, respectively, for Ti (2.5 %)@ZnO, Ti (5 %)@ZnO, Ti (7.5 %)@ZnO, and Ti (10 %)@ZnO. Furthermore, the doping caused the pore volume to rise from 0.0223 to 0.0273 cm^3/g. The pore diameters of Ti (2.5 %)@ZnO, Ti (5 %)@ZnO, Ti (7.5 %)@ZnO, and Ti (10 %)@ZnO were 11.22, 13.18, 13.31, and 14.79 nm, respectively. Based on the results, it is possible to deduce that the addition of Ti to ZnO alters the surface area and the diameter.

X-ray photoelectron spectroscopy (XPS) was used to examine the surface composition of the produced TiO_2@ZnO nanosorbent. The broad-range XPS spectrum (Fig. 4a) reveals the existence of Ti, O, and Zn in the Ti (10 %)@ZnO sample. This proves that any impurities are present in the as-fabricated nanomaterials. Fig. 4b–d depict the high-resolution spectrum of Ti 2p, O 1s, and Zn 2p. The peak at 530.6 eV refers to oxygen in metal oxides, whereas the shoulder peak at 533.2 eV indicates the presence of surface OH groups. The existence of the OH group is attributable to the adsorption of water on the sample surface during air exposure. The deconvoluted Zn 2p spectra revealed Zn 2p1/2 and Zn 2p3/2 peaks at 1022.4 and 1046.4 eV, respectively. These binding energies correspond to Zn–O bonding and imply ZnO production.

The functional groups of the collected samples were recognized using FTIR. Fig. 5a depicts the FTIR spectrum of ZnO doped with different titanium concentrations. The large band at 3500 cm^{-1} may be attributed to the surface O–H stretching vibration hydroxyl groups of nanocomposites. The peaks at 1080 and 1160 cm^{-1} are possibly attributable to the Ti–OH bond [46]. The Zn–O–Ti vibrational mode is marked by the band at 800 cm^{-1} [47], while the wide bands between 500 and 700 cm−1 related to the O–Ti–O bending vibration and the symmetric stretching vibration of the Ti–O–Ti bond [48]. In order to verify the existence of certain crystalline structures, Raman spectroscopy was carried out on the obtained Ti-doped ZnO. Fig. 5b displays the Raman spectra of doped ZnO nanocomposites with Ti concentrations. The existence of a prominent peak at 440 cm^{-1} in all samples is characterized as the E_2^{high} mode of the hexagonal wurtzite ZnO phase, indicating that the doped ZnO nanostructures that were formed had a highly crystalline structure and a hexagonal wurtzite phase [49]. The presence of defects such as Zn interstitials and oxygen vacancies is indicated by the peak at 579 cm^{-1} peak, which corresponds to A1 (LO) mode [49]. The strong Raman signal at 718 cm^{-1} may be linked to a superposition of the A1g mode (612 cm^{-1}) and B2g mode (800 cm^{-1}) superpositions, which agrees with the peak at 692 cm^{-1} formed by a second-order process in rutile single as found by Xing-Yuan et al. [50]. As TiO_2 concentration increased, the intensity of peaks at 440 cm^{-1} decreased, while the peaks at 719 cm^{-1} increased, corresponding to the rutile XRD peak intensity increasing.

3.2. MO and IC dyes adsorption study

3.2.1. Effect of doping loading

Doping concentration plays a crucial role in the adsorption process [17]. To select the most effective nanomaterial samples for dye

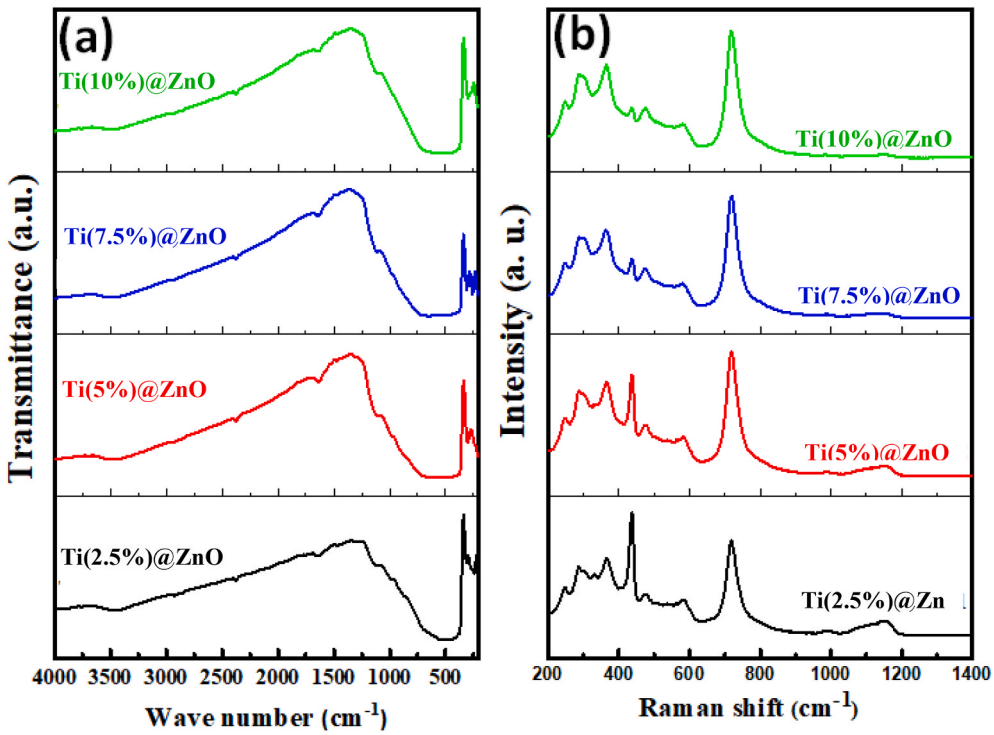

Fig. 5. (a) FTIR and (b) Raman spectra of Ti doped ZnO nanocomposites.

adsorption, doped ZnO NPs with varying Ti concentrations were tested as MO and IC elimination adsorbents. As shown in Fig. 6a, the percentage of MO and IC adsorbed increases with the Ti doping rate up to 98 % and 89 %, respectively. The maximum percentages of dye adsorption were obtained with Ti (10 %)@ZnO, and this is due to its large surface area (15.5 m^2/g from BET results) as well as the lower crystallite size (37.3 nm). Rahali et al. [51] investigated the elimination of CR dye by Ba-doped ZnO NPs with various concentrations of Ba. They concluded that the maximum percentage of CR dye adsorption was obtained for a doping concentration with a large surface area. Therefore, Ti (10 %)@ZnO was selected as the adsorbent for further experimental work.

3.2.2. *Effect of pH*

It is common knowledge that the solution's pH level substantially influences the adsorption of organic dyes [52,53]. The pH analysis was carried out using Ti (10 %)@ZnO nanocomposite with initial dye concentrations of 50 mg/L to make clear how the pH of the solution affects the MO and IC dyes' ability to be removed. As shown in Fig. 6b, it can be noticed that the higher adsorption capacity was reached at pH values equal to 3 and 7 for IC and MO dyes, in that order. Concisely, the adsorption capacity was 103.59 mg. g^{-1} at a pH value equal to 3 for IC and 158.9 mg. g^{-1} for MO at a pH value equal to 7. Then, the capability for adsorption of both dyes was gradually decreased at a pH value higher than 7. Ti (10 %)@ZnO has a zero-charge surface (pHpzc) at a pH value equal to 8, as shown in Fig. 6c. This indicates that in a pH value higher than 8, the Ti (10 %)@ZnO surface is negatively charged. Consequently, anionic dyes and the negatively charged surface of Ti (10 %)@ZnO exhibit electrostatic repulsion. Also, analyzing the impact of pH reveals that the adsorption of IC and MO dyes onto Ti (10 %)@ZnO nanocomposite is regulated by electrostatic attraction. At lower pH values.

3.2.3. *Effect of contact time*

The effect of equilibrium time (contact time) on IC and MO adsorption onto Ti (10 %)@ZnO nanocomposite was investigated. As shown in Fig. 7a and **b**, the elimination rate was impressively quick in the first minutes of time contact (55 min for MO and 52 min for IC), then steadily decreased with time until the equilibrium duration was achieved. The electrostatic attraction of active sites on the Ti (10 %)@ZnO and the dye causes the fast equilibrium rate. Furthermore, the mesoporous Ti (10 %)@ZnO's large surface area allowed facile contact with the organic dye contaminants.

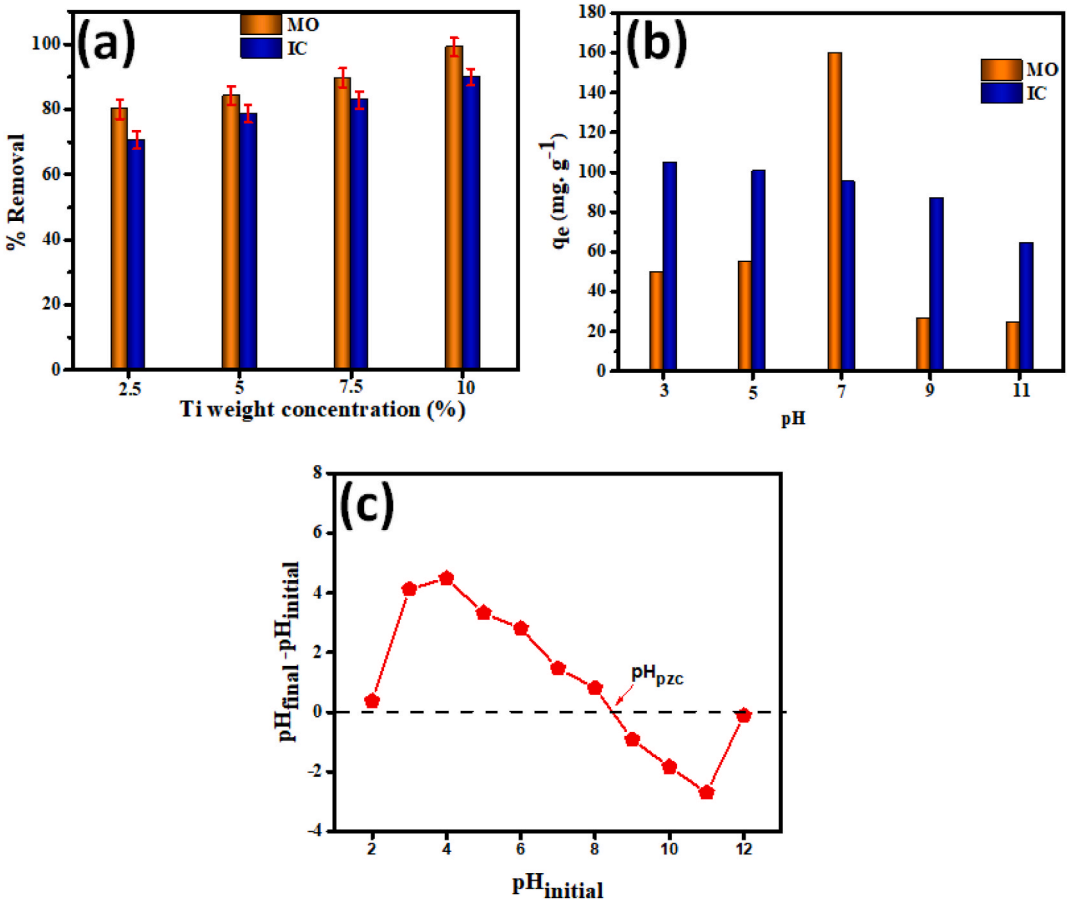

Fig. 6. (a) Influence of Ti weight concentration on % removal of MO and IC (b) influence of pH on elimination efficiency of MO and IC by Ti (10 %)@ZnO nanocomposites and (c) plot for the determination of pHZ of Ti (10 %)@ZnO.

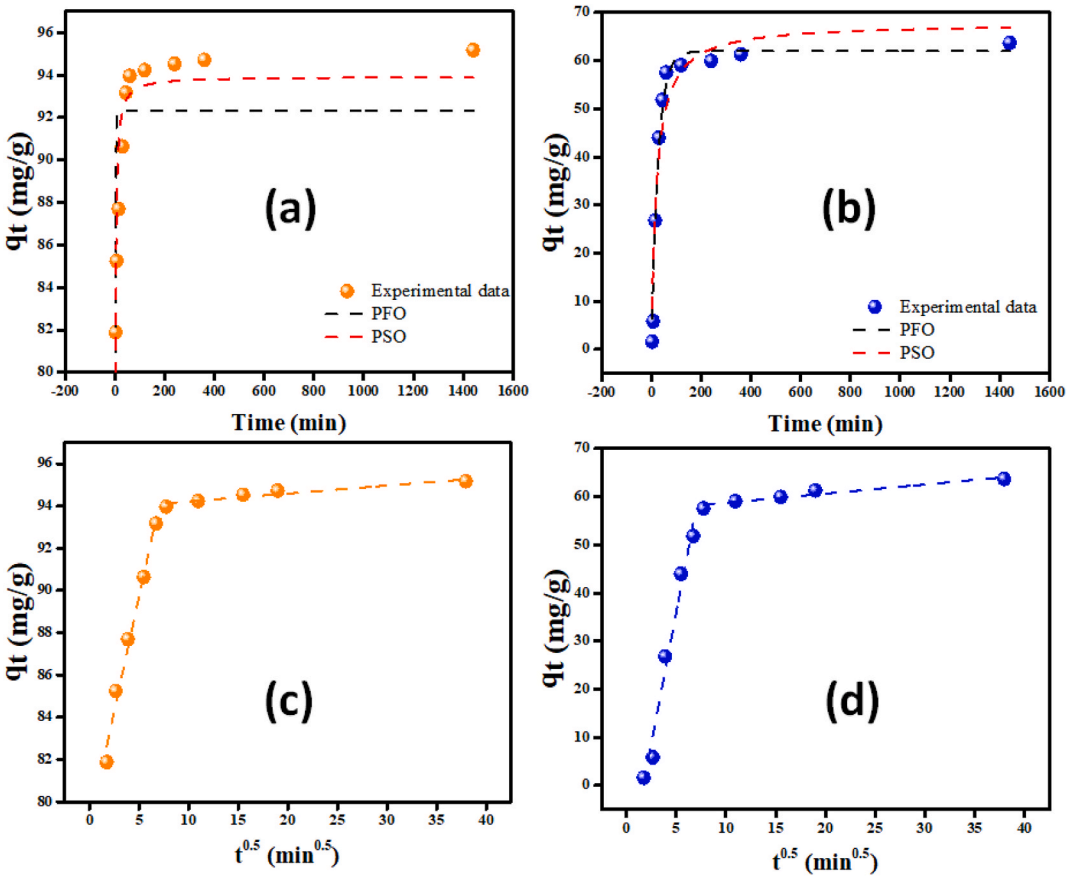

Fig. 7. nonlinear PFO and PSO for the uptake of (a) MO and (b) IC and IPD model for (c) MO and (d) IC onto Ti (10 %)@ZnO nanocomposites.

3.2.4. Kinetic study

The experimental data were modeled with a pseudo-first-order (PFO) (Eq. 7), a pseudo-second-order (PSO) (Eq. 8), and an intraparticle diffusion (ID) (Eq. 9) models to better understand the adsorption process. The PFO model is one of the most frequently utilized models in the liquid phase sorption approach, revealing that physical effects primarily influence the adsorption process [54]. For adsorption adhering to the PSO model, chemical action and not physical migration can be regarded to influence the adsorption process [55]. Table 1 displays the adsorption kinetic parameters and correlation coefficients, and the fitting curve of the adsorption process.

As shown in Table 1, the correlation coefficient value gotten from the PSO plots is higher than that of the PFO model. While the fitting curve of the IC adsorption process is better consistent with the PFO model ($R^2 = 0.976$). These results suggest that the MO adsorption process is controlled and regulated by chemisorption, and physical effects primarily control the adsorption of IC dye onto

Table 1
The adsorption Kinetics models parameters of MO and IC ions onto TiZnO nanoparticles.

Kinetics Models	Equations	Eq. N°	Parameters	MO	IC
PFO	$q_t = q_e(1 - e^{-k_1 t})$	7	q_e	92.32	61.97
			k_1	0.689	0.036
			R^2	0.529	0.976
PSO	$q_t = \frac{t\,k_2 q_e^2}{k_2 q_e t + 1}$	8	$q_{e\ (calculated)}$	93.92	67.82
			k_2	0.02	$7.09^* 10^{-4}$
			R^2	0.87	0.939
IPD	$q_t = k_{dif}\sqrt{t} + C$	9	C_1	78.76	18.93
			K_{dif1}	2.16	10.86
			R^2	0.984	0.976
			C_2	93.84	56.87
			K_{dif2}	0.03	0.18
			R^2	0.910	0.931

nanosorbents [56].

Membrane diffusion and particle diffusion have the greatest influence on the adsorption rate. Fig. 7c and **d** presents the linear fitting of the diffusion model. There are two steps in the adsorption process according to the diffusion model. The initial fast adsorption stage is mostly influenced by membrane diffusion. During this phase, MO and IC dyes is rapidly absorbed by the active site on the Ti (10 %)@ZnO's surface. The greater rate of the first sorption step may be attributed to the dye transfer from the solution to the Ti (10 %) @ZnO surface by the boundary layer. The following step describes the ultimate equilibrium stage, where the intra-particle diffusion decreases owing to the lowest gradient concentration of the dye and the minimal holes and pores accessible to diffusion [57].

3.2.5. *Adsorption isotherm*

By investigating adsorption at equilibrium, important information is provided that aids in identifying adsorbate-adsorbent interactions. Fig. 8a and **b** depict the experimental adsorption isotherms for MO and IC dyes, respectively. Three isotherm models, Langmuir, Freundlich, and Sips were used to examine the equilibrium adsorption data. The parameters of the nonlinear fitting of the Langmuir isotherm (Eq. 10), the Freundlich isotherm (Eq. 11), and the Sips isotherm models (Eq. 12) are described in Table 2.

The results of the non-linear isotherm graphs for MO and IC adsorption onto Ti (10 %)@ZnO nanocomposite are presented in Fig. 8 (a and b), and the obtained isotherm constants are shown in Table 2. It is clear from the isotherm plots and the R^2 values for MO and IC dyes adsorption onto Ti (10 %)@ZnO nanocomposite that the adsorption datum closely resembles the Langmuir adsorption isotherm models. Table 2 shows that the maximum adsorption capability for MO and IC using the Langmuir isotherm model is 994.24 and 305.93 mg. g^{-1}.

3.3. *Adsorption mechanism*

The investigation into the impact of pH suggests that electrostatic attraction may be the primary factor governing the adsorption mechanism of MO and IC dyes onto Ti (10 %)@ZnO. At higher pH values, the Ti (10 %)@ZnO surface and the anionic dyes (MO and IC) exhibited similar charges, which hindered the adsorption of dyes due to electrostatic repulsions. The observed adsorption efficiency at pH > pHpzc provides evidence for the presence of additional interactions between anionic dyes (MO and IC) and Ti (10 %)@ZnO. It is possible that hydrogen bonding, hydrophobic interactions, pore diffusion, and π–π interaction are involved in the process of MO and IC dye adsorption onto Ti (10 %)@ZnO nanocomposite [17,26]. To deepen our understanding of the adsorption mechanism of MO and IC dyes to Ti (10 %)@ZnO, FTIR analysis was conducted before and after adsorption to confirm the interaction between the nanocomposite and organic dyes. Fig. 9a and b illustrates the FTIR spectra of MO and IC dyes after and before adsorption onto the Ti (10 %) @ZnO. The distinctive bands of MO and IC dye are also observed in the spectra after, with slight modifications in position, as illustrated in Fig. 9a and b. Furthermore, the stretching O–H band shifts owing to the creation of H-bonding between the amine groups of MO and IC molecules and the OH groups on the surface of Ti (10 %)@ZnO nanocomposite. The MO and IC anionic dyes and Ti (10 %)@ZnO surfaces were oppositely charged at low pH values, enhancing MO and IC adsorption owing to the electrostatic attraction.

Furthermore, earlier research has revealed that the most optimal conditions for adsorption are those in which the adsorbent's pore width is either 1.2 or 1.7 times the adsorbate's widest [60]. The MO and IC longitudinal length are about 1.5 nm and 0.9 nm [61,62], respectively, which is less than the pore diameter of Ti (10 %)@ZnO, which is 14.79 nm as depicted from BET results, showing that Ti (10 %)@ZnO can adsorb MO and IC dyes via the pore filling mechanism. The suggested adsorption mechanism of the MO and IC onto the Ti (10 %)@ZnO nanocomposites involves electrostatic attractions, hydrogen bonds, and pore diffusion (Fig. 10 a).

3.4. *Recycling performance*

One of the most important criteria for determining the practical value of an adsorbent is its re-recovery performance, which

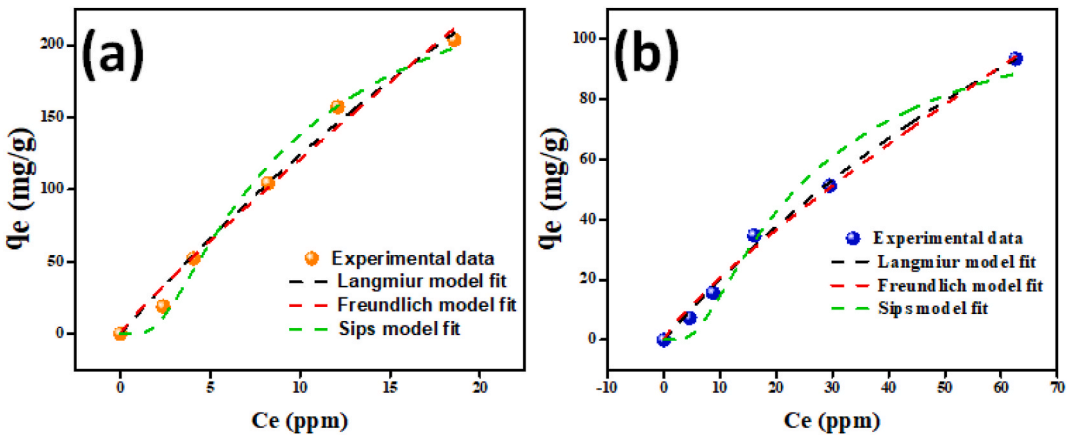

Fig. 8. Non-linear adsorption isotherms of (a) MO and (b) IC dyes onto Ti (10 %)@ZnO nanocomposite.

Table 2
Different equilibrium Isotherms' constants for MO and IC adsorption by Ti (10 %)@ZnO nanocomposite.

Equilibrium Model	Equations model	Eq N°	Parameters	MO	IC
Langmuir	$q_e = \frac{q_m K_L C_e}{1 + K_L C_e}$ [58]	**10**	**qm** (mg. g^{-1})	994.24	305.39
			$\mathbf{K_L}$ (mg. g^{-1})	0.001	0.007
			$\mathbf{R_L}$ ($L.mg^{-1}$)	0.901	0.588
			$\mathbf{R^2}$	0.989	0.996
Freundlich	$q_e = k_F C_e^{\frac{1}{n}}$ [59]	**11**	N	1.101	0.828
			$\mathbf{K_F}$ ($L.mg^{-1}$)	15.49	3.06
			$\mathbf{R^2}$	0.979	0.991
Sips	$q_e = \frac{q_m K_s C_e^{1/n}}{1 + K_s C_e^{1/n}}$	**12**	$\mathbf{q_m}$ **(mg. g^{-1})**	302.71	125.22
			$\mathbf{K_s}$ **($L.mg^{-1}$)**	15.09	5.54
			n	119.01	120.17
			$\mathbf{R^2}$	0.972	0.971

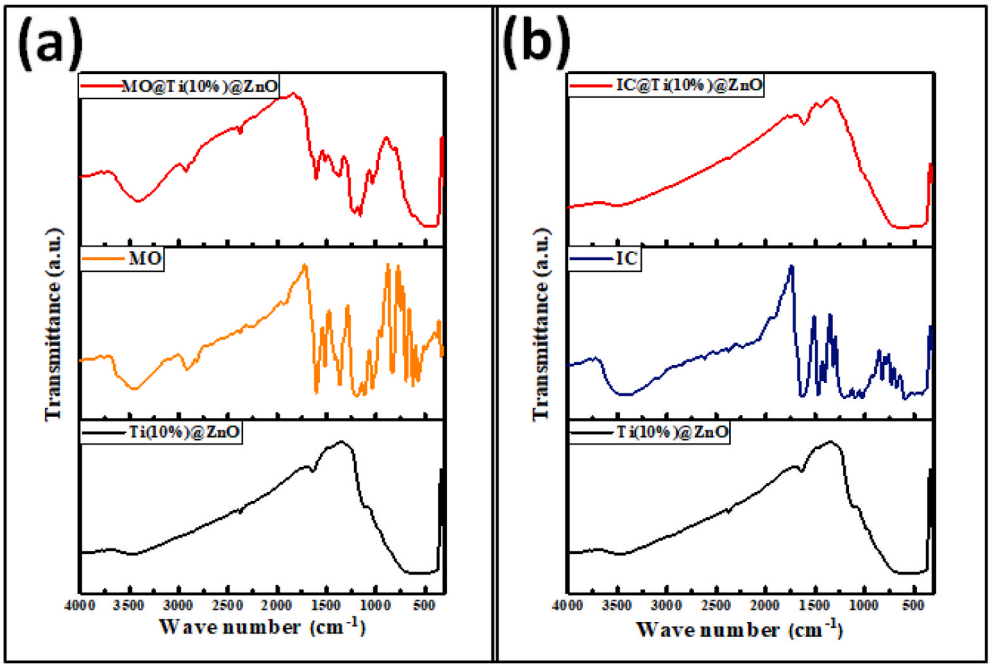

Fig. 9. FTIR spectra of Ti (10 %)@ZnO nanocomposite before and after adsorption of (a) MO and (b) IC dyes.

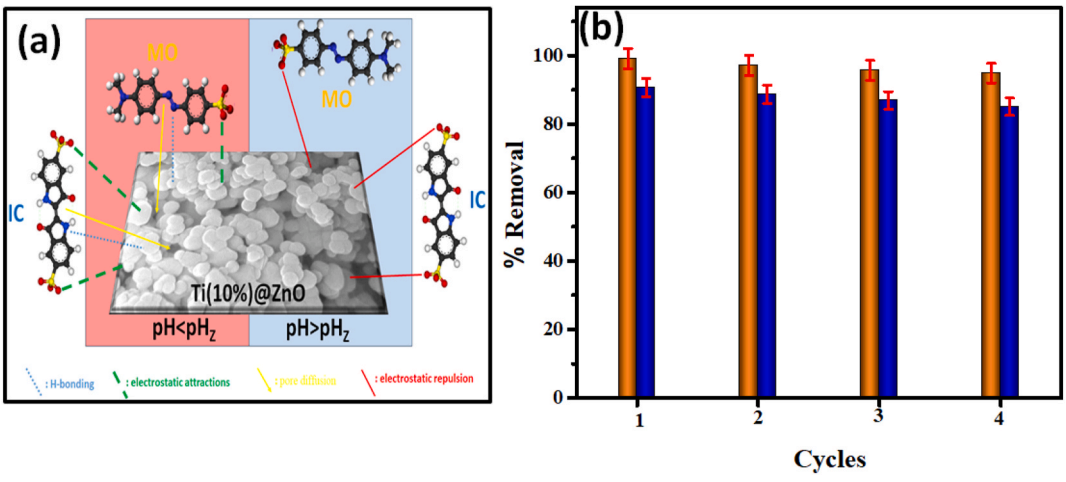

Fig. 10. (a) Suggested removal mechanism of MO and IC by Ti (10 %)@ZnO and (b) Reusability study of Ti (10 %)@ZnO.

Table 3
A comparative analysis of the IC and MO dyes adsorbed Ti (10 %)@ZnO and those reported in the literature.

Adsorbents	Dyes	Adsorption capacity (mg. g^{-1})	Contact time (min)	References
ZnO-orange peel	MO	166.25	–	[63]
ZnO@AC	MO	107.97	–	[63]
ZnO-NPs	MO	65.2	120	[64]
ZnO@AC composite from wood sawdust	MO	42.61	60	[65]
CN–Fe_2O_3NPs	MO	527.83	53	[14]
Carbon nanotubes	IC	93.00	50	[66]
Montmorillonite	IC	40.00	20	[67]
Chitosan aerogels	IC	168.60	100	[68]
$MgFe_2O_4$	IC	46	60	[69]
MgOBi2	IC	126	74	[17]
Ti (10 %)@ZnO	MO	994.24	52	This work
Ti (10 %)@ZnO	IC	305.39	55	This work

determines the cost of using the adsorbent. The Ti (10 %)@ZnO cyclic availability must then be verified. After the MO and IC dye adsorption experiment, the Ti (10 %)@ZnO nanocomposite was filtered and calcined at 500 °C for 1 h. The recovered Ti (10 %)@ZnO was then reused. Fig. 10 b depicts the Ti (10 %)@ZnO reusability performance. Ti (10 %)@ZnO was found to be engaged in at least four continuous cycles for MO and IC dye removal.

Various materials have been employed in the literature to eliminate IC and MO dyes from aqueous solutions. As shown in Table 3, our absorbent's competitiveness was evaluated compared to other reported adsorbents. The adsorbents in our study exhibited competitive adsorption ability and affinity compared to the other adsorbents towards IC and MO dyes. In addition, the adsorbents that we have developed exhibit cost-effectiveness when designed for practical applications. Therefore, Ti (10 %)@ZnO composite is strongly suggested as an effective adsorbent for anionic dyes. This is attributed to their straightforward synthesis, efficacy, and reusability, which are advantageous for treating effluents that contain dyes, including those used in the textile industry.

4. Conclusion

TiO_2 doping ZnO nano-sorbents with various doping weight concentrations (2.5, 5, 7.5, and 10 %) were successfully synthesized via a simple sonication method. The obtained nano-sorbents were characterized by FESEM, BET, XRD, XPS, RAMAN, and FTIR techniques. The nano-sorbents were specifically designed to remove MO and IC dyes from wastewater. Doping concentration, contact time, and pH were all evaluated as adsorption parameters. The outcomes revealed that the Ti (10 %)@ZnO nano-sorbent has a higher surface area of 15.5 m^2/g and pore diameters of 14.79 nm, fast adsorption equilibrium for MO and IC dyes in less than 55 min, and the adsorption capacity of the Ti (10 %)@ZnO nano-sorbent was determined to be 994.24 mg/g for MO and 305.39 mg/g for IC dye. The Langmuir isotherm model was found to be the best fit for the MO and IC adsorption process. The suggested MO and IC adsorption mechanism onto the Ti (10 %)@ZnO nanocomposite involves electrostatic attractions, hydrogen bonds, and pore diffusion, as FTIR and pH analysis indicated. The reusability tests show that Ti (10 %)@ZnO nano-sorbent has the potential to be used to remove MO and IC dyes from an aqueous solution after four cycles. This study reveals that Ti (10 %)@ZnO nano-sorbent can efficiently and promptly remove anionic dyes such as MO and IC from aqueous solutions. For future research, an investigation of the TiO_2 doped ZnO_2 will be needed to treat other pollutants in the wastewater.

Funding

This work was supported and funded by the Deanship of Scientific Research at Imam Mohammad Ibn Saud Islamic University (IMSIU) through Research Partnership Program (grant number IMSIU-RP23086).

Data availability

The datasets used and/or analyzed in the current investigation will be made available by the corresponding author upon reasonable request.

CRediT authorship contribution statement

Mohamed Ali Ben Aissa: Writing – original draft, Methodology, Investigation, Conceptualization. **M. Khairy:** Writing – original draft, Methodology, Funding acquisition, Conceptualization. **Magdi E. Khalifa:** Investigation, Funding acquisition, Conceptualization. **Ehab A. Abdelrahman:** Methodology, Investigation. **Nadeem Raza:** Methodology, Investigation. **Emad M. Masoud:** Methodology, Investigation. **Abueliz Modwi:** Methodology, Investigation.

Declaration of competing interest

The authors declare that they have no known competing financial interests or personal relationships that could have appeared to influence the work reported in this paper.

Acknowledgement

The authors extend their appreciation to the Deanship of Scientific Research at Imam Mohammad Ibn Saud Islamic University (IMSIU), Saudi Arabia for funding and supporting this work through Research Partnership Program (grant number IMSIU-RP23086).

References

[1] B.J. Singh, A. Chakraborty, R. Sehgal, A systematic review of industrial wastewater management: Evaluating challenges and enablers, J. Environ. Manag. 348 (2023) 119230, https://doi.org/10.1016/j.jenvman.2023.119230.
[2] C. Zhang, G. Zhao, Y. Jiao, B. Quan, W. Lu, P. Su, Y. Tang, J. Wang, M. Wu, N. Xiao, Critical analysis on the transformation and upgrading strategy of Chinese municipal wastewater treatment plants: towards sustainable water remediation and zero carbon emissions, Sci. Total Environ. (2023) 165201, https://doi.org/10.1016/j.scitotenv.2023.165201.
[3] F. Kordbacheh, G. Heidari, Water pollutants and approaches for their removal, Materials Chemistry Horizons 2 (2023) 139–153, https://doi.org/10.22128/MCH.2023.684.1039.
[4] F. Keshavarzi, M.R. Samaei, H. Hashemi, A. Azhdarpoor, A. Mohammadpour, Application of montmorillonite/octadecylamine nanoparticles in the removal of textile dye from aqueous solutions: Modeling, kinetic, and equilibrium studies, Heliyon (2024) e25919, https://doi.org/10.1016/j.heliyon.2024.e25919.
[5] O. Tomin, R. Vahala, M.R. Yazdani, Synthesis and efficiency comparison of reed straw-based biochar as a mesoporous adsorbent for ionic dyes removal, Heliyon 10 (2024) e25919, https://doi.org/10.1016/j.heliyon.2024.e24722.
[6] M. Faheem, M.A. Hassan, T. Mehmood, F. Al-Misned, N.K. Niazi, J. Bao, J. Du, Super capacity of ligand-engineered biochar for sorption of malachite green dye: key role of functional moieties and mesoporous structure, Environ. Sci. Pollut. Control Ser. (2024) 1–17, https://doi.org/10.1007/s11356-024-32897-8.
[7] S. Dutta, S. Adhikary, S. Bhattacharya, D. Roy, S. Chatterjee, A. Chakraborty, D. Banerjee, A. Ganguly, S. Nanda, P. Rajak, Contamination of textile dyes in aquatic environment: Adverse impacts on aquatic ecosystem and human health, and its management using bioremediation, J. Environ. Manag. 353 (2024) 120103, https://doi.org/10.1016/j.jenvman.2024.120103.
[8] K. Sharma, S. Chakroborty, K. Pal, A.R. Panda, J. Malviya, N. Nath, T. Yadav, A.S. Parmar, L. Parmar, N. Asthana, Controllable synthesis of high-yield magnetic nanomaterials assisted dye adsorbents from waste-water treatment and applications, J. Mol. Struct. (2024) 137550, https://doi.org/10.1016/j.molstruc.2024.137550.
[9] B.E. Keshta, H. Yu, L. Wang, MIL series-based MOFs as effective adsorbents for removing hazardous organic pollutants from water, Separ. Purif. Technol. (2023) 124301, https://doi.org/10.1016/j.jhazmat.2022.128271.
[10] A. Modwi, M.R. Elamin, B.Y. Abdulkhair, N.Y. Elamin, M.A.B. Aissa, R.B. Said, Synthesis and characterization of Ti-dopedY2O3@ C3N4 nanocomposite for the removal of dyes from aqueous solution, Inorg. Chem. Commun. (2023) 111594, https://doi.org/10.1016/j.inoche.2023.111594.
[11] K. Jing, X. Liu, T. Liu, Z. Wang, H. Liu, Facile and green construction of carboxymethyl cellulose-based aerogel to efficiently and selectively adsorb cationic dyes, J. Water Proc. Eng. 56 (2023) 104386, https://doi.org/10.1016/j.jwpe.2023.104386.
[12] W.M.B.D.A. Abd, A. Troush, Equilibrium and kinetic studies of Biosorption of methyl orange dye from aqueous solution onto Dodonaea Angustifolia (sand olive) tree. https://doi.org/10.13140/RG.2.2.15653.93923, 2016.
[13] K. Wang, Y. Kou, K. Wang, S. Liang, C. Guo, W. Wang, Y. Lu, J. Wang, Comparing the adsorption of methyl orange and malachite green on similar yet distinct polyamide microplastics: uncovering hydrogen bond interactions, Chemosphere 340 (2023) 139806, https://doi.org/10.1016/j.chemosphere.2023.139806.
[14] C.A. Mbachu, A.K. Babayemi, T.C. Egbosiuba, J.I. Ike, I.J. Ani, S. Mustapha, Green synthesis of iron oxide nanoparticles by Taguchi design of experiment method for effective adsorption of methylene blue and methyl orange from textile wastewater, Results in Engineering 19 (2023) 101198, https://doi.org/10.1016/j.rineng.2023.101198.
[15] I.A. Al-Baldawi, S.R.S. Abdullah, A.F. Almansoory, N.I. Ismail, H.A. Hasan, N. Anuar, Role of Salvinia molesta in biodecolorization of methyl orange dye from water, Sci. Rep. 10 (2020) 13980, https://doi.org/10.1038/s41598-020-70740-5.
[16] A. Aljuaid, M. Almehmadi, A.A. Alsaiari, M. Allahyani, O. Abdulaziz, A. Alsharif, J.A. Alsaiari, M. Saih, R.T. Alotaibi, I. Khan, g-C3N4 based photocatalyst for the efficient photodegradation of toxic methyl orange dye: recent modifications and future perspectives, Molecules 28 (2023) 3199, https://doi.org/10.3390/molecules28073199.
[17] F.A. Adam, M. Ghoniem, M. Diawara, S. Rahali, B.Y. Abdulkhair, M. Elamin, M.A.B. Aissa, M. Seydou, Enhanced adsorptive removal of indigo carmine dye by bismuth oxide doped MgO based adsorbents from aqueous solution: equilibrium, kinetic and computational studies, RSC Adv. 12 (2022) 24786–24803, https://doi.org/10.1039/D2RA02636H.
[18] X. Zhang, G. Mao, Y. Jiao, Y. Shang, S. Han, Technology, Adsorption of Anionic Dye on Magnesium Hydroxide-Coated Pyrolytic Bio-Char and Reuse by Microwave Irradiation. 11, 2014, https://doi.org/10.1007/s13762-013-0338-5, 1439-1448.
[19] A.N. Babu, D.S. Reddy, P. Sharma, G.S. Kumar, K. Ravindhranath, P. Mohan, Removal of Hazardous Indigo Carmine Dye from Waste Water Using Treated Red Mud, 17, 2019, pp. 198–208, https://doi.org/10.1016/j.matpr.2019.06.419.
[20] B. Debina, S.N. Eric, D. Fotio, K.T. Arnaud, D.-Y. Lemankreo, S. Rahman, C. Engineering, Adsorption of Indigo Carmine Dye by Composite Activated Carbons Prepared from Plastic Waste (PET) and Banana Pseudo Stem 8 (2020) 39–55, https://doi.org/10.4236/msce.2020.812004.
[21] V.S. Mane, I.D. Mall, m. Srivastava, Kinetic and Equilibrium Isotherm Studies for the Adsorptive Removal of Brilliant Green Dye from Aqueous Solution by Rice Husk Ash. 84, 2007, pp. 390–400, https://doi.org/10.1016/j.jenvman.2006.06.024.
[22] M.A.B. Aissa, A. Modwi, K. Taha, N. Elamin, R.A. AbuMousa, M. Bououdina, Environmental remediation applications of MxOy-gC3N4 nanocomposites (M= Mg, Ti, and Zn): photocatalytic activity for Indigo carmine dye degradation, Diam. Relat. Mater. 136 (2023) 109988, https://doi.org/10.1016/j.diamond.2023.109988.
[23] M.G. Ghoniem, M.A. Ben Aissa, F.A. Adam, W.M. Daoush, M. Khairy, Photocatalytic decomposition of Congo red dye by black paste@ TiO2 as an efficient recyclable photocatalyst, Z. Naturforsch. (2023), https://doi.org/10.1515/zna-2023-0142.
[24] R.B. Said, S. Rahali, M.A. Ben Aissa, A. Albadri, A. Modwi, Uptake of BF dye from the aqueous phase by CaO-g-C3N4 nanosorbent: construction, descriptions, and recyclability, Inorganics 11 (2023) 44, https://doi.org/10.3390/inorganics11010044.
[25] N. Elamin, A. Modwi, M.B. Aissa, K.K. Taha, O.K. Al-Duaij, T. Yousef, Fabrication of Cr–ZnO photocatalyst by starch-assisted sol–gel method for photodegradation of Congo red under visible light, J. Mater. Sci. Mater. Electron. 32 (2021) 2234–2248, https://doi.org/10.1007/s10854-020-04988-y.
[26] L. Khezami, M.A.B. Aissa, A. Modwi, A. Guesmi, F.K. Algethami, M. Bououdina, Efficient removal of organic dyes by Cr-doped ZnO nanoparticles, Biomass Conversion and Biorefinery (2022) 1–14, https://doi.org/10.1007/s13399-022-02952-w.
[27] M. Ben Aissa, L. Khezami, K. Taha, N. Elamin, B. Mustafa, A. Al-Ayed, A. Modwi, Yttrium oxide-doped ZnO for effective adsorption of basic fuchsin dye: equilibrium, kinetics, and mechanism studies, Int. J. Environ. Sci. Technol. (2021) 1–14, https://doi.org/10.1007/s13762-021-03816-y.
[28] M. Andrade-Guel, C. Cabello-Alvarado, P. Bartolo-Pérez, D. Medellin-Banda, C. Ávila-Orta, B. Cruz-Ortiz, A. Espinosa-Muñoz, G.C. Pliego, Surface modification of TiO 2/ZnO nanoparticles by organic acids with enhanced methylene blue and rhodamine B dye adsorption properties, RSC advances 12 (2022) 28494–28504, https://doi.org/10.1039/D2RA04961A.

[29] N. Tripathy, R. Ahmad, H. Kuk, D.H. Lee, Y.-B. Hahn, G. Khang, Rapid methyl orange degradation using porous ZnO spheres photocatalyst, J. Photochem. Photobiol. B Biol. 161 (2016) 312–317, https://doi.org/10.1016/j.jphotobiol.2016.06.003.

[30] T. Naseem, T. Durrani, The role of some important metal oxide nanoparticles for wastewater and antibacterial applications: a review, Environmental Chemistry and Ecotoxicology 3 (2021) 59–75, https://doi.org/10.1016/j.enceco.2020.12.001.

[31] A. Das, B.N. Chowdhury, R. Saha, S. Sikdar, S. Bhunia, S. Chattopadhyay, Ultrathin vapor–liquid–solid grown titanium dioxide-II film on bulk GaAs substrates for advanced metal–oxide–semiconductor device applications, IEEE Trans. Electron. Dev. 65 (2018) 1466–1472, https://doi.org/10.1109/TED.2018.2802490.

[32] H. Safajou, H. Khojasteh, M. Salavati-Niasari, S. Mortazavi-Derazkola, Enhanced photocatalytic degradation of dyes over graphene/Pd/TiO2 nanocomposites: TiO2 nanowires versus TiO2 nanoparticles, J. Colloid Interface Sci. 498 (2017) 423–432, https://doi.org/10.1016/j.jcis.2017.03.078.

[33] A. Menazea, N.S. Awwad, Antibacterial activity of TiO2 doped ZnO composite synthesized via laser ablation route for antimicrobial application, J. Mater. Res. Technol. 9 (2020) 9434–9441, https://doi.org/10.1016/j.jmrt.2020.05.103.

[34] R. Sarathi, N. Sheeba, E.S. Essaki, S.M. Sundar, Titanium doped Zinc Oxide nanoparticles: a study of structural and optical properties for photocatalytic applications, Mater. Today: Proc. 64 (2022) 1859–1863, https://doi.org/10.1016/j.matpr.2022.06.387.

[35] M. Kumar, R. Ravikumar, M. Rao, Structural, optical, and photoluminescence studies of Ti-doped ZnO nanopowders by a simple solution method, J. Appl. Spectrosc. (2022) 1–8, https://doi.org/10.1007/s10812-022-01363-z.

[36] K. Siwińska-Stefańska, A. Kubiak, A. Piasecki, A. Dobrowolska, K. Czaczyk, M. Motylenko, D. Rafaja, H. Ehrlich, T. Jesionowski, Hydrothermal synthesis of multifunctional TiO2-ZnO oxide systems with desired antibacterial and photocatalytic properties, Appl. Surf. Sci. 463 (2019) 791–801, https://doi.org/10.1016/j.apsusc.2018.08.256.

[37] A. Modwi, M. Abbo, E. Hassan, A. Houas, Effect of annealing on physicochemical and photocatalytic activity of Cu 5% loading on ZnO synthesized by sol–gel method, J. Mater. Sci. Mater. Electron. 27 (2016) 12974–12984, https://doi.org/10.1007/s10854-016-5436-y.

[38] C.A. De León-Condés, G. Roa-Morales, G. Martínez-Barrera, C. Menchaca-Campos, B. Bilyeu, P. Balderas-Hernández, F. Ureña-Núñez, H.P. Toledo-Jaldin, Sulfonated and gamma-irradiated waste expanded polystyrene with iron oxide nanoparticles, for removal of indigo carmine dye in textile wastewater, Heliyon 5 (2019) e02071, https://doi.org/10.1016/j.heliyon.2019.e02071.

[39] L. Khezami, K.K. Taha, A. Modwi, Efficient removal of cobalt from aqueous solution by zinc oxide nanoparticles: kinetic and thermodynamic studies, Z. Naturforsch. 72 (2017) 409–418, https://doi.org/10.1515/zna-2016-0477.

[40] A. Modwi, M. Abbo, E. Hassan, O. Al-Duaij, A. Houas, Adsorption kinetics and photocatalytic degradation of malachite green (MG) via Cu/ZnO nanocomposites, J. Environ. Chem. Eng. 5 (2017) 5954–5960, https://doi.org/10.1016/j.jece.2017.11.024.

[41] M. Ismail, A. Albadri, M.A. Ben Aissa, A. Modwi, S.M. Saleh, High poisonous Cd ions removal by Ru-ZnO-g-C3N4 nanocomposite: description and adsorption mechanism, Inorganics 11 (2023) 176, https://doi.org/10.3390/inorganics11040176.

[42] R. Ade, S.S. Kumar, S. Valanarasu, S.S. Kumar, S. Sasikumar, V. Ganesh, Y. Bitla, H. Algarni, I. Yahia, Enhanced optoelectronic properties of Ti-doped ZnO nanorods for photodetector applications, Ceram. Int. 47 (2021) 24031–24038, https://doi.org/10.1016/j.ceramint.2021.05.112.

[43] C.-L. Hsu, Y.-D. Gao, Y.-S. Chen, T.-J. Hsueh, Vertical Ti doped ZnO nanorods based on ethanol gas sensor prepared on glass by furnace system with hotwire assistance, Sensor. Actuator. B Chem. 192 (2014) 550–557, https://doi.org/10.1016/j.snb.2013.11.024.

[44] X. Bokhimi, A. Morales, F. Pedraza, Crystallography and crystallite morphology of rutile synthesized at low temperature, J. Solid State Chem. 169 (2002) 176–181, https://doi.org/10.1016/S0022-4596(02)00046-4.

[45] M.A. Al-Ghouti, D.A. Da'ana, Guidelines for the use and interpretation of adsorption isotherm models: a review, J. Hazard Mater. 393 (2020) 122383, https://doi.org/10.1016/j.jhazmat.2020.122383.

[46] T. Lopez, E. Sanchez, P. Bosch, Y. Meas, R. Gomez, FTIR and UV-Vis (diffuse reflectance) spectroscopic characterization of TiO2 sol-gel, Mater. Chem. Phys. 32 (1992) 141–152, https://doi.org/10.1016/0254-0584(92)90270-I.

[47] S. Moradi, P. Aberoomand-Azar, S. Raeis-Farshid, S. Abedini-Khorrami, M.H. Givianrad, The effect of different molar ratios of ZnO on characterization and photocatalytic activity of TiO2/ZnO nanocomposite, J. Saudi Chem. Soc. 20 (2016) 373–378, https://doi.org/10.1016/j.jscs.2012.08.002.

[48] K. Karthik, S.K. Pandian, N.V. Jaya, Effect of nickel doping on structural, optical and electrical properties of TiO2 nanoparticles by sol–gel method, Appl. Surf. Sci. 256 (2010) 6829–6833, https://doi.org/10.1016/j.apsusc.2010.04.096.

[49] T. Ahmad, V. Pandey, M.S. Husain, S. Munjal, Structural and spectroscopic analysis of pure phase hexagonal wurtzite ZnO nanoparticles synthesized by sol-gel, Mater. Today: Proc. 49 (2022) 1694–1697, https://doi.org/10.1016/j.matpr.2021.07.456.

[50] G. Xing-Yuan, X. Da-Peng, D. Zhan-Hui, S. Wen-Hui, Preparation and Raman spectrum of rutile single crystals using floating zone method, Chin. Phys. Lett. 23 (2006) 1645, https://doi.org/10.1088/0256-307X/23/6/080.

[51] S. Rahali, M.A. Ben Aissa, L. Khezami, N. Elamin, M. Seydou, A. Modwi, Adsorption behavior of Congo red onto barium-doped ZnO nanoparticles: correlation between experimental results and DFT calculations, Langmuir 37 (2021) 7285–7294, https://doi.org/10.1021/acs.langmuir.1c00378.

[52] M.G. Ghoniem, F.A.M. Ali, B.Y. Abdulkhair, M.R.A. Elamin, A.M. Alqahtani, S. Rahali, M.A. Ben Aissa, Highly selective removal of cationic dyes from wastewater by MgO nanorods, Nanomaterials 12 (2022) 1023, https://doi.org/10.3390/nano12061023.

[53] M.A. Ben Aissa, A. Modwi, A.E. Albadri, S.M. Saleh, Dependency of crystal violet dye removal behaviors onto mesoporous V2O5-g-C3N4 constructed by simplistic ultrasonic method, Inorganics 11 (2023) 146, https://doi.org/10.3390/inorganics11040146.

[54] J. Wang, X. Guo, Adsorption kinetic models: physical meanings, applications, and solving methods, J. Hazard Mater. 390 (2020) 122156, https://doi.org/10.1016/j.jhazmat.2020.122156.

[55] J. Wang, W. Cai, R. Zuo, C. Du, A study of Sr sorption behavior in claystone from a candidate high-level radioactive waste geological disposal site under the action of FeOOH colloids, Int. J. Environ. Res. Publ. Health 19 (2022) 9970, https://doi.org/10.3390/ijerph19169970.

[56] S. Wei, A.R. Kamali, Waste plastic derived Co3Fe7/CoFe2O4@ carbon magnetic nanostructures for efficient dye adsorption, J. Alloys Compd. 886 (2021) 161201, https://doi.org/10.1016/j.jallcom.2021.161201.

[57] I. Ali, C. Peng, T. Ye, I. Naz, Sorption of cationic malachite green dye on phytogenic magnetic nanoparticles functionalized by 3-marcaptopropanic acid, RSC Adv. 8 (2018) 8878–8897, https://doi.org/10.1039/C8RA00245B.

[58] L. Khezami, A. Modwi, I. Ghiloufi, K.K. Taha, M. Bououdina, A. ElJery, L. El Mir, Effect of aluminum loading on structural and morphological characteristics of ZnO nanoparticles for heavy metal ion elimination, Environ. Sci. Pollut. Control Ser. 27 (2020) 3086–3099, https://doi.org/10.1007/s11356-019-07279-0.

[59] H. Freundlich, Over the adsorption in solution, J. Phys. Chem 57 (1906) 1100–1107.

[60] Q.-S. Liu, T. Zheng, P. Wang, J.-P. Jiang, N. Li, Adsorption isotherm, kinetic and mechanism studies of some substituted phenols on activated carbon fibers, Chemical engineering journal 157 (2010) 348–356, https://doi.org/10.1016/j.cej.2009.11.013.

[61] J. Wang, W. Chen, M. Zhang, R. Zhou, J. Li, W. Zhao, L. Wang, Optimize the preparation of Fe 3 O 4-modified magnetic mesoporous biochar and its removal of methyl orange in wastewater, Environ. Monit. Assess. 193 (2021) 1–20, https://doi.org/10.1007/s10661-021-08971-w.

[62] W. Krieger, M. Hoerbelt, S. Schuster, J. Hennekes, N. Kockmann, Kinetic study of leuco-indigo carmine oxidation and investigation of Taylor and Dean flow superposition in a coiled flow inverter, Chem. Eng. Technol. 42 (2019) 2052–2060, https://doi.org/10.1002/ceat.201800753.

[63] W. Ahlawat, N. Dilbaghi, R. Kumar, N.K. Singhal, A. Kaushik, S. Kumar, Adsorption of harmful dyes and antimicrobial studies utilizing recyclable ZnO, its composites with conventionally used activated carbon, and waste orange peel as a greener approach, J. Environ. Chem. Eng. 11 (2023) 110268, https://doi.org/10.1016/j.jece.2023.110268.

[64] M.N. Zafar, Q. Dar, F. Nawaz, M.N. Zafar, M. Iqbal, M.F. Nazar, Effective adsorptive removal of azo dyes over spherical ZnO nanoparticles, J. Mater. Res. Technol. 8 (2019) 713–725, https://doi.org/10.1016/j.jmrt.2018.06.002.

[65] N.S. Sayed, A.S. Ahmed, M.H. Abdallah, G.A. Gouda, ZnO@ activated carbon derived from wood sawdust as adsorbent for removal of methyl red and methyl orange from aqueous solutions, Sci. Rep. 14 (2024) 5384, https://doi.org/10.1038/s41598-024-55158-7.

[66] M.R. Elamin, B.Y. Abdulkhair, A.O. Elzupir, Removal of ciprofloxacin and indigo carmine from water by carbon nanotubes fabricated from a low-cost precursor: solution parameters and recyclability, Ain Shams Eng. J. 14 (2023) 101844, https://doi.org/10.1016/j.asej.2022.101844.

[67] F. Geyikçi, Factorial design analysis for adsorption of Indigo Carmine onto Montmorillonite-Evaluation of the kinetics and equilibrium data, Prog. Org. Coating 98 (2016) 28–34, https://doi.org/10.1016/j.porgcoat.2016.04.019.
[68] M.S. de Luna, C. Ascione, C. Santillo, L. Verdolotti, M. Lavorgna, G. Buonocore, R. Castaldo, G. Filippone, H. Xia, L. Ambrosio, Optimization of dye adsorption capacity and mechanical strength of chitosan aerogels through crosslinking strategy and graphene oxide addition, Carbohydrate polymers 211 (2019) 195–203, https://doi.org/10.1016/j.carbpol.2019.02.002.
[69] M. Adel, M.A. Ahmed, A.A. Mohamed, Effective removal of indigo carmine dye from wastewaters by adsorption onto mesoporous magnesium ferrite nanoparticles, Environ. Nanotechnol. Monit. Manag. 16 (2021) 100550, https://doi.org/10.1016/j.enmm.2021.100550.